EPR-correlated dipolar spectroscopy by Q-band chirp SIFTER

Andrin Doll, Gunnar Jeschke

Supplementary Information

1. Q-band AWG spectrometer

As mentioned in the main text, the Q-band extension to our X-band AWG spectrometer has the same overall architecture as the X-band transceiver described in [1, 2]. The actual signal routing is therefore very similar and modifications are mostly related to different microwave components being used at Q band. A schematic layout is shown in Fig. S1 and the components are listed in Table S1. As compared to X band, the most significant change in signal routing is that the up-conversion of AWG pulses is performed with an IQ mixer instead of a single mixer (M_1). As a consequence of that, two channels of the AWG in quadrature phase relation are required.
With the LO frequency being tunable, the instantaneous detection bandwidth of 1 GHz can be adjusted within the frequency window from 33 GHz to 36 GHz. An adjustable frequency window is important at Q band, because there is a considerable spread in operation frequencies due to the different resonator designs and sample properties. One drawback of this adjustable frequency window is, however, that rejection of image frequencies by high-pass filters with fixed cutoff frequencies is no longer suitable. For up-conversion, such a filter is in principle not needed due to the IQ mixer, which is designed to reject image frequencies. However, by testing our signal quality experimentally using the test procedure detailed previously (see Fig. S.4 in [3]), we found that the second harmonic of the AWG coupled rather well to our frequency window of interest. As long as the excitation pulses are bound to the 1-2 GHz frequency window available for detection, as in the presented experiments, spurious excitation is no an issue. However, for the broad bandwidths required for population transfer in high-spin systems [3], the currently used excitation arm is not yet clean enough. To overcome this limitation, a two-stage up-conversion scheme will be implemented, where the critical first up-conversion step can be performed at a fixed LO frequency. For down-conversion, the absence of image rejection results in noise contributions to the detected signal which originate from

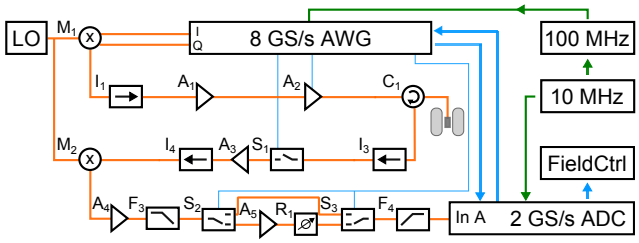

Figure S1: Layout of the home-built AWG spectrometer at Q band showing the main signal path (orange), hardware triggers with controlled timing (blue), and clock signals (green). The components are listed in Table S1. Microwave attenuators with fixed attenuation levels, for instance to level signal amplitudes, are not shown in the scheme.

Label	Device
AWG	Agilent/Keysight M8190A with options 002, 12G, AMP, SEQ, FSW, 02G IQ pairs from Ch 1 and Ch 2 are differential outputs converted to single-ended by two Picosecond 5310A Balun
ADC	SP Devices ADQ412-4G PCIe
FieldCtrl	Bruker E32
M_1	IQ mixer assembled of Marki ML1-1040LS mixer (2x) Marki QH-0444 quadrature hybrid Marki PD-0140 combiner
M_2	Marki ML1-1040LS
I_1, I_4	Raditek Rad-34-36-K1
I_3	Wenteq F3336-3450-10
C_1	Wenteq F3836-3450-03
A_1	3J GAC-333620KF
A_2	Applied Systems Engineering TWT 187KA
A_3	3J LNAC-333630KF
A_4	Minicircuits ZX60-V62
A_5	Herotek AF01-6362513B
S_1	Herley F9014-9
S_2, S_3	Minicircuits ZASWA-2-50DR
R_1	Minicircuits ZX76-15R5-PP-5+
F_3	Minicircuits SLP-2400
F_4	Minicircuits SHP-900+
LO	Agilent E8257D frequency-doubled by Marki ADA1020 (33 GHz - 36 GHz)
CLK	Nexyn NXOS-PLXO-100-03593 (10 MHz → 100 MHz) Agilent E8257D 10 MHz RefClk (Master for ADC and all derived clocks)

Table S1: Component listing for spectrometer layout in Figure S1.

the lower sideband. This is actually the reason why the current Q-band spectrometer is slighly worse in terms of SNR for very small signals than a recent commercial Q-band spectrometer available in our lab (data not shown). By incorporation of image rejection into down-conversion, we expect the SNR with our Q-band spectrometer to become competitive with commercial spectrometers for identical experiments. Notably, we already incorporated image rejection into our X-band spectrometer, where we did indeed achieve competitive sensitivity compared to a recent commercial spectrometer available in our lab (unpublished results).

2. Dipolar evolution for chirp SIFTER

2.1. Understanding the modulation formula

The formulas for the dipolar evolution detected on S_1 and S_2 share a common phase evolution term, whose phase is given by

$$\phi_{\text{principal}} = \omega_{\text{dd}}(\tau_1 - \tau_2 + \delta_1/2 - \delta_{12}/2) \tag{1}$$

Importantly, this evolution phase can be followed throughout the pathway that starts by excitation of S_1 and finishes by detection of S_2. This is the upper of the two evolution pathways shown in Fig. 3 in the main text. For the first evolution during the τ_1 periods, the maximum (principal) evolution phase for S_1 is $\phi_{1,\text{max}} = \omega_{\text{dd}}(\tau_1 - \delta_{12}/2)$. This is solely determined by the time period between excitation of S_2 by pulse ① and excitation of S_1 by pulse ③. Note the start at the excitation of S_2 due to the partial refocusing of the dipole-dipole interaction that adds the $\cos(\omega_{\text{dd}}\delta_{12}/2)$ factor to the final modulation formula. By taking into consideration pulse ②, one sees that part of the maximum principal phase is refocused, so that the principal phase acquired in the τ_1 periods is

$$\phi_1 = \omega_{\text{dd}}(\tau_1 - 3\delta_{12}/2) \tag{2}$$

In the time period of duration δ_{12} between excitation of S_1 and S_2 by pulse ③, no evolution takes place since both coupled spins are aligned longitudinally (longitudinal two-spin order of the type $2\hat{S}_{1,z}\hat{S}_{2,z}$). Only the evolution of S_2 between pulse ③ and the echo therefore needs to be considered for the remaining evolution period. Here, one finds $\phi_{2,\text{max}} = \omega_{\text{dd}}(\tau_2 - \delta_1/2 - \delta_{12}/2)$, which reduces to

$$\phi_2 = \omega_{\text{dd}}(\tau_2 - \delta_1/2 - \delta_{12}) \tag{3}$$

due to refocusing by pulse ④. As is readily verified, $\phi_{\text{principal}} = \phi_1 - \phi_2$. For the pathway detected on S_1, these basic considerations therefore allow to fully rationalize the final modulation formula. For the other pathway, which starts by excitation of S_2 and finishes by detection of S_1, we could not obtain such an understanding. In particular, the transfer of anti-phase coherence from S_2 to S_1 by pulse ③ results in pathways involving multi-quantum coherence, which complicates such an analysis.

2.2. Spread in evolution phases

To analyze the spread due to the distribution of the resonance offset as well as due to the multiple evolution pathways, the SIFTER modulation formulas reported in the main text are fully expanded. For the more complicated of the two pathways, we also include the factor that depends on $(\tau_1 + \tau_2)$ without expansion, which has been omitted in the main text. Accordingly, the modulation formula for S_1 is

$$\left\langle \hat{S}_{y,1} \right\rangle (t_{\text{det}}) = \frac{6}{8} \cos\left(\omega_{\text{dd}}(\tau_1 - \tau_2 + \delta_1/2 - \delta_{12}/2)\right) \tag{4}$$

$$+ \frac{1}{8} \cos\left(\omega_{\text{dd}}(\tau_1 - \tau_2 + \delta_1/2 - 3\delta_{12}/2)\right) \tag{5}$$

$$+ \frac{1}{8} \cos\left(\omega_{\text{dd}}(\tau_1 - \tau_2 + \delta_1/2 + \delta_{12}/2)\right) \tag{6}$$

$$+ \frac{2}{8} \cos\left(\omega_{\text{dd}}(\tau_1 + \tau_2 - \delta_1/2 - 5\delta_{12}/2)\right) \cdot \left(\cos\left(\omega_{\text{dd}}\delta_{12}\right)\right) - 1) \tag{7}$$

Considering the additional pathway that depends on $(\tau_1 + \tau_2)$, its contribution vanishes for $\delta_{12} \ll 1/\omega_{\text{dd}}$. For S_2, the modulation formula is

$$\left\langle \hat{S}_{y,2} \right\rangle (t_{\text{det}}) = \frac{1}{2} \cos\left(\omega_{\text{dd}}(\tau_1 - \tau_2 + \delta_1/2)\right) \tag{8}$$

$$+ \frac{1}{2} \cos\left(\omega_{\text{dd}}(\tau_1 - \tau_2 + \delta_1/2 - \delta_{12})\right) \tag{9}$$

Using the same parameters as in Fig. 2b in the main text, the spread in dipolar evolution times of all pathways is shown in Fig. S2, where panel (a) shows the pathways detected on S_1 and panel (b) the pathways detected on S_2. Note that the green curve corresponds to the principal evolution pathway in Eq. (1) of this SI. For this principal pathway, the overall spread is 50 ns, which is comparable to the 2 : 1 chirp echo analyzed in the main text. However, the different dependencies of each pathway on δ_{12} broaden the distribution. This effect is most pronounced for the pathway corresponding to term (5) in Eqs. (4)-(7). A conservative estimation for the overall spread in evolution times is therefore 100 ns, which corresponds to a frequency of 10 MHz.

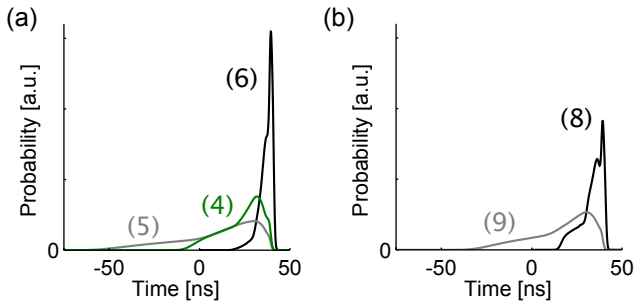

Figure S2: Evolution times at $t = \tau_1 - \tau_2 = 0$ for the various pathways in SIFTER detected on the first spin S_1 (a) and on the second spin S_2 (b). The numbers in brackets are the references to the patway in the equations given above. The same parameters as in Fig. 2b in the main text were used. The y-axes of the two plots are the same, so that (a) and (b) can be directly compared in terms of probability amplitude.

With distances beyond 3.7 nm, dipolar frequencies ω_{dd} are still five times slower.

It is presumed that the actual limit under our conditions is below 3.7 nm. Notably, a rather similar situation is encountered in DEER with a chirp pump pulse. In recent experiments [4], for instance, we could faithfully measure a mean distance of 3.4 nm using two consecutive 64 ns pump pulses. Since the pulses used in DEER were resonant with the pumped spins during the entire pulse duration, this translates to a total spread in evolution times by 128 ns. In another experiment using a single 64 ns pump pulse [5], examination on a spacer with mean distance of 2.4 nm revealed interference for dipolar frequencies above 4.7 MHz. Since each of these DEER experiments had its own characteristic distribution of evolution times, comparison amongst different experiments is not straightforward. Nevertheless, we would expect from these results that SIFTER under our experimental conditions is not significantly affected by interference down to 3.4 nm. Given that we neglected the low weighting factors of the two pathways that correspond to Eqs. (5) and (6), experiments are likely to turn out to be unproblematic even down to 3 nm or slightly below. Importantly, long δ_{12} delays contribute most significantly to the spread in evolution times. As a consequence of that, interference at short distances will be most pronounced for spin partners having a large resonance offset.

3. Supplementary experimental data

3.1. Pulse excitation profiles

In the main text, we concluded from Fig. 1b that our excitation pulses are largely uniform. In order to confirm this by an independent experiment, the excitation profile of the first pulse was recorded experimentally. In order to obtain such an excitation profile, longitudinal magnetization upon the pulse of interest is detected at various observation frequencies [1]. Three profiles are shown in Fig. S3a, illustrating a bandwidth-compensated chirp (black), a non-compensated chirp (orange), as well as a 2.75 ns long monochromatic pulse (blue). As is readily seen, the bandwidth-compensated pulse achieves the most uniform excitation profile. This is because the bandwidth compensation establishes a flip angle β_{LZSM} that is formally independent on frequency offset [5]. The non-compensated chirp as well as the monochromatic pulse both show the fingerprint of the resonator response function in their excitation profiles. For the 250 MHz broad nitroxide spectrum, both of these pulses result in considerable variation of the flip angle throughout the spectrum.

Notably, both these non-compensated pulses would achieve fairly uniform excitation profiles over 250 MHz if there would be no limitation in excitation bandwidth due to the microwave resonator. In such an idealized situation, one could also readily identify the characteristic excitation profiles of a linear frequency sweep and of a short monochromatic pulse. In presence of bandwidth limitations, however, these non-compensated pulses will no longer reproduce the excitation profile under idealized conditions. The reason why the excitation profiles of the non-compensated pulses of different type have a rather comparable shape in Fig. S3a can be justified by linear response theory. In fact, the assumption of linear response of spin excitation explains why the FT of the excitation pulse inside the resonator translates into the excitation profile $M_z(f)$ displayed in Fig. S3a. The assumption of linear response of the excitation electronics explains why the FT of the excitation pulse inside the resonator has its shape determined by the resonator profile. For completeness, the FT of the compensated chirp pulse as seen by the spins is shown in black in Fig. S3b. The most prominent variations observed in the experimental excitation profile around 35 GHz are actually already contained in that FT. Note that the pronounced curvature of the FT of the chirp pulse as synthesized by the AWG (gray) is due to the variable sweep rate. This sweep rate is calculated such as to compensate for the experimental resonator profile (green).

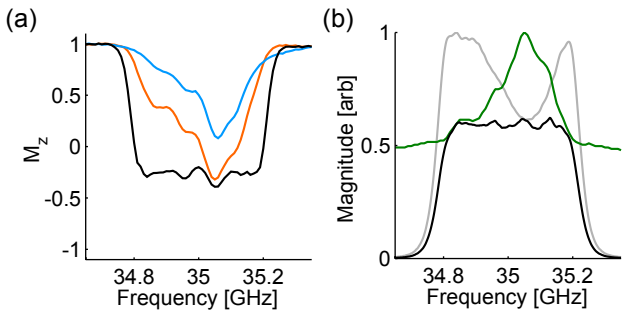

Figure S3: Uniformity of excitation pulses. (a) Comparison of experimental excitation profiles of various coherence excitation pulses with the TEMPOL sample. Black: Bandwidth-compensated chirp, orange: uncompensated constant-rate chirp, blue: monochromatic rectangular pulse with 2.75 ns duration. (b) Self-consistency check of pulse compensation [1]. The black curve is the FT of the pulse as seen by the spins, which is the pulse output by the AWG (gray) convoluted by the experimental resonator profile (green).

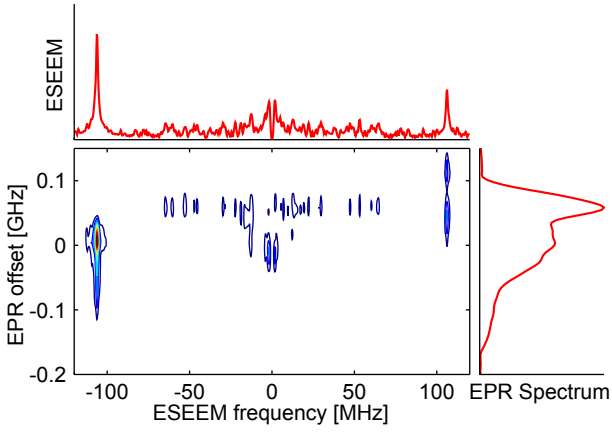

Figure S4: 2D EPR/ESEEM correlation spectrum of the TEMPOL sample. Pulse delays extended up to delays $\tau = 2.34$ μs, starting from $\tau = 0.35$ μs with an increment in τ of 2 ns.

3.2. Q-band chirp ESEEM

As one would expect, ESEEM due to matrix protons is suppressed at Q-band as compared to X-band. Nevertheless, 2:1 chirp echoes with the 1 mM TEMPOL solution showed proton modulations of a few percent. The modulation frequencies are visualized by the 2D EPR/ESEEM correlation spectrum in Fig. S4. The most significant modulation is actually at 106 MHz, which corresponds to the proton double frequency. The fundamental frequency may not be resolved here due to broadening mechanisms [6]. Using three-pulse chirp ESEEM [7], it was possible to detect a weak signature of the fundamental frequency (data not shown).

3.3. Additional SIFTER data

The modulation averaging procedure implemented in SIFTER is visualized in Fig. S5. Here, each of the colored traces represents one of the 12 datasets recorded at a different $2(\tau_1 + \tau_2)$ setting, with the shortest setting resulting in the red curve at the top. The modulation-averaged trace is shown in black. The larger residual modulation at the end of the trace as compared to the residual modulation at the beginning of the trace is readily seen for the red curve at the top.

For the 2D correlation spectrum shown in the main text, we mentioned that spectral quality could here be improved by apodization along the SIFTER dimension t. To visualize the effect of this apodization, Fig. S6 shows 2D spectra obtained with (a) and without (b) apodization. The most apparent improvements are around the dipolar zero frequency. Moreover, there are less contributions at EPR offsets related to the background signal from quarz. Overall, the contour lines are also less noisy, since the apodization suppresses noise originating from the unmodulated parts of the time-domain signal. However, the window also suppresses some of the extended modulations around the Pake singularities, which introduces artificial broadening of the dipolar spectrum. This broadening is apparent for the horns of the Pake pattern sum projection and for the red region in the contour plots. This is also the reason why such an apodization is not recommended if dipolar modulations extend throughout the entire time window.

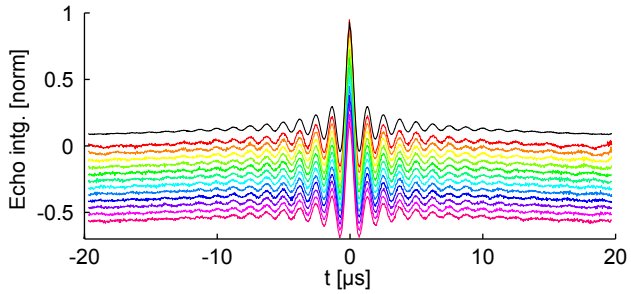

Figure S5: Averaging of residual modulations by incrementing $2(\tau_1 + \tau_2)$. The black curve is the averaged trace and corresponds to the data shown in Fig. 4 in the main text. The colored curves are the 12 datasets at different $2(\tau_1 + \tau_2)$ settings, with a 392 ns increment from trace to trace, starting from the red curve at the top.

Another important aspect in the dipolar 1D projection without apodization is that there is no considerable contribution at half the dipolar frequency. Such half-frequency artefacts would be seen if the residual half-frequency modulations were not averaged out. From the dipolar 1D projection with apodization, one could not draw such a conclusion, since the window would suppress eventual half-frequency artifacts.

References

[1] A. Doll, G. Jeschke, Fourier-transform electron spin resonance with bandwidth-compensated chirp pulses, J. Magn. Reson. 246 (2014) 18 – 26.

[2] G. Jeschke, S. Pribitzer, A. Doll, Coherence transfer by passage pulses in electron paramagnetic resonance spectroscopy, J. Phys. Chem. B 119 (2015) 13570–13582.

[3] A. Doll, M. Qi, S. Pribitzer, N. Wili, M. Yulikov, A. Godt, G. Jeschke, Sensitivity enhancement by population transfer in Gd(III) spin labels, Phys. Chem. Chem. Phys. 17 (2015) 7334–7344.

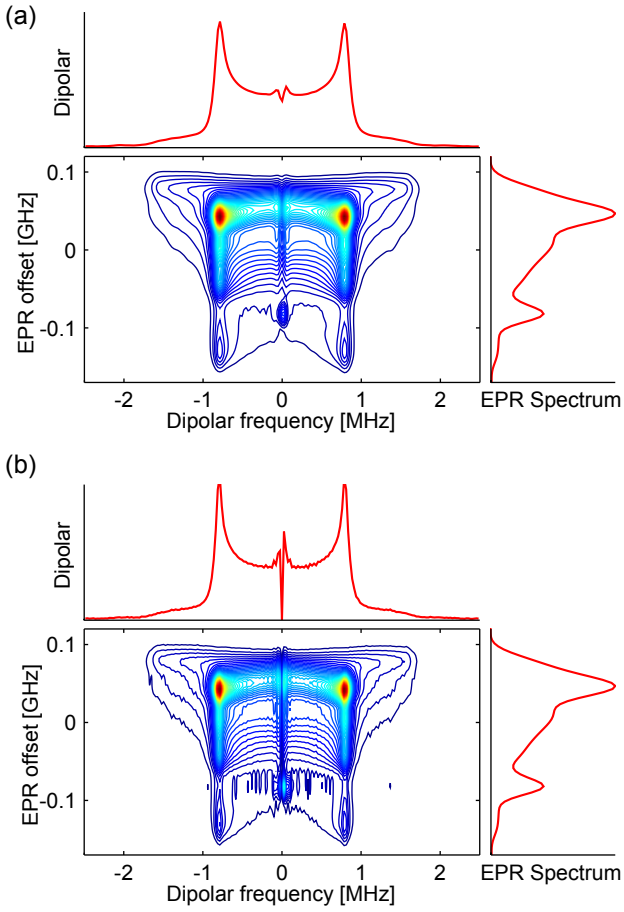

Figure S6: EPR-correlated SIFTER data with (a) and without (b) apodization by a Chebychev window centered around $t = 0$ of the time-domain SIFTER traces.

[4] A. Doll, M. Qi, N. Wili, S. Pribitzer, A. Godt, G. Jeschke, Gd(III)-Gd(III) distance measurements with chirp pump pulses, J. Magn. Reson. 259 (2015) 153 – 162.

[5] A. Doll, S. Pribitzer, R. Tschaggelar, G. Jeschke, Adiabatic and fast passage ultra-wideband inversion in pulsed EPR, J. Magn. Reson. 230 (2013) 27 – 39.

[6] V. Yudanov, K. Salikhov, G. Zhidomirov, Y. D. Tsvetkov, Effect of the magnetic nuclei of a matrix to the form of decay in spin-echo signal in free radicals, J. Strukt. Khim 10 (1969) 732–734.

[7] T. F. Segawa, A. Doll, S. Pribitzer, G. Jeschke, Copper ESEEM and HYSCORE through ultra-wideband chirp EPR spectroscopy, J. Chem. Phys. 143 (2015) 044201.